Title

Growth of encapsulating carbon on supported Pt nanoparticles studied by in situ TEM

Authors

Wu, Jason
Helveg, Stig
Ullmann, Sven
et al.

Publication Date

2016-06-01

DOI

10.1016/j.jcat.2016.03.010

Journal of Catalysis 338 (2016) 295–304

Contents lists available at ScienceDirect

Journal of Catalysis

journal homepage: www.elsevier.com/locate/jcat

Growth of encapsulating carbon on supported Pt nanoparticles studied by *in situ* TEM

Jason Wu [a], Stig Helveg [b], Sven Ullmann [b], Zhenmeng Peng [a,c], Alexis T. Bell [a,*]

[a] *Department of Chemical and Biomolecular Engineering, University of California, Berkeley, CA 94720, United States*
[b] *Haldor Topsoe A/S, Haldor Topsøes Allé 1, DK-2800 Kgs. Lyngby, Denmark*
[c] *Department of Chemical and Biomolecular Engineering, University of Akron, Akron, OH 44325, United States*

ARTICLE INFO

Article history:
Received 8 December 2015
Revised 6 March 2016
Accepted 7 March 2016
Available online 1 April 2016

Keywords:
Catalyst deactivation
Coking
Pt
Nanoparticles
In situ TEM
Coking mechanism

ABSTRACT

Carbon deposition on MgO-supported Pt nanoparticles from ethylene decomposition was studied by *in situ* transmission electron microscopy (TEM) at the atomic level. An imaging strategy was established for controlling beam-gas-sample interactions that minimizes beam-induced changes of the reaction. Using this strategy, it was possible to observe how carbon encapsulation occurs on Pt nanoparticles and the role of the Pt surface morphology. The evidence suggests that multiple partial layers grew simultaneously prior to full encapsulation of the nanoparticle. The growth of carbon on Pt nanoparticles was found to induce significant changes in the nanoparticle shape, resulting in particles becoming rounder as coking progressed. Closer examination of the surface structure revealed that in some cases carbon growth induced step formation.

1. Introduction

Supported platinum nanoparticles are used extensively to promote the transformation of alkanes to a variety of products via reactions such as dehydrogenation [1–5], dehydroaromatization [6,7], and isomerization [8,9]. These processes are often accompanied by formation of carbonaceous deposits that lead to blockage of the active sites and ultimately to catalyst deactivation [2,10–12]. Extensive research has been undertaken to minimize the deposition of carbon, in an effort to improve the stability of supported Pt nanoparticles. For example, the addition of elements, such as Sn or In, to form a bimetallic catalyst has been found to inhibit coke formation [1–3,13,14]. The use of a support free of acidic sites is also important to prevent coking, since acid sites promote the formation of coke via the polymerization of alkenes and aromatic species produced by the metal [15,16].

Because coke formation on Pt is an important problem, considerable effort has been devoted to characterizing coke formed under different conditions and developing an understanding of the factors that affect coke formation on Pt and Pt bimetallic nanoparticles [17–20]. Transmission electron microscopy (TEM) has proven to be a particularly informative technique for this purpose because it enables visualization of the relationship of the coke with respect to the Pt nanoparticles with atomic resolution and can provide insights into the processes involved in the nucleation and growth of carbon. Most TEM observations of coking have been conducted *ex situ*, i.e., after coke deposition onto the catalyst [20–23]. The development of techniques for obtaining TEM images of catalysts in the presence of a low pressure of hydrocarbon gas (1–10 mbar) and at elevated temperatures [24–27] has opened the way for making *in situ* observations of carbon growth as a function of time [20,28–34]. Because nanoscale carbon has been recognized as a class of materials with interesting physical and chemical properties [35], the majority of carbon deposition studies utilizing *in situ* TEM have focused on metal substrates, such as Ni, Fe, and Co, that favor the formation of graphene and structural derivatives [28–34].

Previous *in situ* TEM observations of carbon nanofiber growth catalyzed by Ni nanoparticles reveal that step sites act as preferential growth centers for graphene on Ni [28]. Density functional theory (DFT) calculations show that the step-mediated growth occurs due to the stronger binding energy of carbon atoms to the steps than to the facets [28,36,37]. The TEM and DFT findings also reveal that a surface diffusion mechanism represents a sufficient account for carbon transport from the adsorption site at the free Ni surface to sites governing the growth of carbon layers [28,38,39], as opposed to earlier proposals that attribute the atom transport to a bulk solubility and diffusion of carbon [31,40]. In contrast to

---

* Corresponding author. Fax: +1 510 642 4778.
E-mail address: bell@cchem.berkeley.edu (A.T. Bell).

http://dx.doi.org/10.1016/j.jcat.2016.03.010
0021-9517/

studies of carbon growth on 3d transition metals, only a few *in situ* studies have been reported for Pt [20,41,42]. Platinum nanoparticles can catalyze the formation of carbon nanofibers [20,41]. Because of the low solubility of carbon in Pt [43], it has been speculated that carbon deposition on Pt similarly proceeds through a surface diffusion mechanism [41,42] and this mechanism may thus explain the growth of individual carbon layers in nanofiber structures as for Ni [28]. Moreover carbonaceous layers can also encapsulate Pt nanoparticles [20]. Encapsulation of 3d metal nanoparticles by multiple carbon layers has been proposed to occur via precipitation of carbon dissolved in the bulk of the nanoparticle at lower temperatures [44]. However, in view of the low solubility of carbon in Pt, it remains an open question pertaining to how multiple carbon layers form on top of each other and what the role of the Pt surface is during carbon encapsulation. To address this issue, the onset of carbon growth and the initial encapsulation of Pt nanoparticles by multiple layers of carbonaceous matter are examined by means of *in situ* TEM.

In the present study, *in situ* TEM was employed to study Pt nanoparticles in the presence of ethylene at elevated temperatures. Ethylene decomposition over Pt nanoparticles is of particular industrial importance because ethylene is the primary source for coke formation on Pt catalysts during the ethane dehydrogenation reaction as shown by isotopic studies [45]. Time-resolved TEM images were acquired in order to directly observe how multiple carbon shells grow upon particle encapsulation, and to address the role of the nanoparticle surface. Despite the impressive capability of *in situ* TEM to monitor carbon formation on working catalysts with atomic scale resolution, beam-induced processes remain challenging. Both elastic scattering and inelastic scattering of electrons are prominent in the presence of gas molecules, causing changes in the catalyst particles and reaction environment that can alter the carbon growth reaction [27,46]. Therefore, a careful investigation of the carbon deposition reaction was carried out in which the electron illumination was systematically optimized to establish an approach allowing for conducting the experiments with suppressed electron beam-induced changes while elucidating the mechanism by which Pt nanoparticles coke at high spatial resolution.

2. Experimental

2.1. Synthesis of Pt/MgO by colloidal method

Platinum nanoparticles were synthesized by reduction of a platinum acetylacetonate ($Pt(acac)_2$, 97%, Aldrich) dissolved in octyl ether (OE, 99%, Aldrich) by 1,2-hexadecanediol (HDD, 90%, Aldrich) in the presence of oleylamine (OAm, 70%, Aldrich) and oleic acid (OA, 99%, Aldrich) [47]. All of the components were added to a 25 ml three-necked flask attached to a Schlenk line and the resulting solution was heated to 563 K at a rate of 2 K/min and maintained at this temperature for 30 min before cooling down to room temperature. The product nanoparticles were then washed by adding a large amount of anhydrous ethanol in order to aid the separation of the Pt nanoparticles. The particle suspension was then centrifuged at 3000 rpm for 1 min and the organics involved in the particle synthesis were removed by decanting the supernatant liquid. The solid material produced in this manner was re-dispersed in anhydrous toluene to form a stable colloidal suspension.

Magnesium oxide (MgO) nanocubes were used as a support in the experiments and were made by re-crystallizing MgO nanopowders (<50 nm, Aldrich) in air at 1333 K for 30 min. A suspension of Pt particles in anhydrous toluene, containing 0.01 g Pt metals in 5 mL of anhydrous toluene, was mixed with a suspension of 0.2 g of MgO in 10 mL of anhydrous toluene. The mixture was stirred overnight under a N_2 atmosphere before the resulting product was precipitated out by adding an excess amount of anhydrous ethanol followed by centrifugation. The solid material was calcined in air at 573 K for 1 h to remove residual organic agents involved in the synthetic procedure and then treated in an atmosphere of 10% H_2/Ar at 873 K for 1 h to fully reduce the Pt surface. The final catalyst was stored in a glovebox (<0.1 ppm O_2, <0.1 ppm H_2O) until further use. This colloidal sample is exhibited in Figs. 2–4, 6–8 and 11, and S2.

2.2. Synthesis of Pt/MgO by wet impregnation method

An additional sample of Pt/MgO was prepared by wet impregnation in order to obtain a sample with larger particle size. Platinum acetylacetonate ($Pt(acac)_2$, 97%, Aldrich) was dissolved in toluene and added to slurry of MgO in toluene to achieve a Pt content of 3.5 wt%. The mixture was then stirred at room temperature for 2 h and then set in a rotary evaporator overnight to remove the solvent. After drying, the catalyst was reduced at 723 K for 2 h (5 K/min ramp) in a flow of 10% H_2/Ar to form the final catalyst. The final catalyst was stored in a glovebox (<0.1 ppm O_2, <0.1 ppm H_2O) until further use. This impregnated sample is exhibited in Figs. 10 and S1.

2.3. Ex situ TEM characterization and reactor testing

Samples were first examined by *ex situ* TEM to characterize particle size and loading. Images were taken using a FEI Tecnai 12 transmission electron microscope with an accelerating voltage of 120 kV at the Electron Microscope Laboratory of the University of California, Berkeley. High-resolution TEM (HRTEM) characterizations of the samples were conducted on the TEAM 0.5 high-resolution microscope operated at 80 kV at the National Center for Electron Microscopy (NCEM).

A portion of the catalyst synthesized by colloidal method was used for *ex situ* carbon deposition in a reactor system in order to provide a reference point for optimizing electron beam illumination. In a typical procedure, 25 mg of catalyst was loaded into a quartz tube reactor and heated to 873 K at 15 K/min in 20% H_2/He using a three-zone furnace at 1 atm. The catalyst was maintained at this temperature for 1 h before being exposed to a feed of 40% C_2H_6/He, at a flow rate of 40 cm^3/min. The reaction was then stopped by cooling the sample down to room temperature in the gas flow, and the coked catalyst was stored in a vacuum desiccator.

2.4. In situ TEM

In situ TEM experiments were carried out using an image aberration-corrected Titan 80-300 ETEM microscope equipped with a differentially pumped gas cell [46]. The microscope was operated in the TEM mode at an acceleration voltage of 300 kV, with the spherical aberration coefficient in the range of -10 to -20 μm and electron dose-rates of 100–2000 $e^-/(\text{Å}^2\ s)$ in the magnification range that allowed for resolving the lattice spacing of Pt (1 1 1) and Pt(2 0 0) lattice planes. Specimens were prepared by crushing the dry catalyst powders, dispersing it in anhydrous ethanol, and casting droplets of the solution on either plasma-cleaned stainless steel grids or Protochips E-chips. Stainless steel grids were mounted in a Gatan 628 Inconel single-tilt heating holder. The temperature was measured by a thermocouple attached to the furnace of the holder [48]. The E-chips were loaded into the Protochips MEMS-based heating holder. The E-chips were operated at elevated temperatures using a constant-resistance mode [49]. Specifically, the relationship between the temperature and electrical biasing was previously calibrated by the manufacturer

(Protochips) for the range of 293–1473 K in a base pressure of 1.3×10^{-2} mbar. Therefore, in the presence of gas, the actual temperature of the heating membrane will be lower, corresponding to a higher resistance. For the present experiments, E-chips were first heated to a nominal temperature in vacuum and the resistance was recorded. Upon introduction of gas, the biasing was adjusted to keep the resistance at the value recorded in vacuum and thus maintaining the temperature.

In any experiments, an as-prepared specimen was first reduced by heating in 1 mbar H_2 to 773 K for 30 min, after which specific particles were selected for time-resolved observations. The deposition of carbon was initiated by the removal of hydrogen, adjustment of the temperature in vacuum to the growth condition, introduction of 1 mbar ethylene and finally readjusting the resistance matching the calibrated vacuum temperature. Once the specimen drift had subsided, time-lapsed TEM image series were acquired of nanoparticles during the exposure to ethylene. The single TEM images were acquired by illuminating a charge-coupled device camera for 0.1–1 s to the electron beam. In order to minimize beam-induced artifacts in the *in situ* observations, the specimen was illuminated at low electron dose-rates [46] and the electron beam was blanked off in between successive images to minimize the total accumulated electron dose delivered to the specimen areas under observation. In order to estimate the total accumulated electron dose, the amount of time spent illuminating each nanoparticle for locating, focusing and imaging the specimen area was recorded, which varied between 2 and 4 min per image. The signal-to-noise ratio (S/N) was calculated as the mean pixel count divided by its standard deviation in a region of the image without sample. Following the experiment, the reaction gas was removed from the microscope and a post-mortem examination of the specimen was conducted at a pressure below 1×10^{-5} mbar and at either 773 K or a lower temperature. Fig. 1 illustrates the imaging strategy including the three modes of data collection. In Mode 1, particles are observed after reduction, during growth, and after growth. In Mode 2, particles are only observed after reduction and after growth, with no illumination to the beam during ethylene exposure. Finally, in Mode 3, particles are observed post-mortem in vacuum without any previous beam illumination.

3. Results and discussion

Fig. 2a shows a TEM image of the as-synthesized Pt nanoparticles dispersed on a carbon-coated copper grid, together with a particle size distribution. Most of the Pt particles were faceted in shape and had an average diameter of 5.9 ± 1.6 nm. The Pt nanoparticles were deposited onto the MgO support and the material was subsequently calcined in order to remove the capping agents, reduced in H_2 *ex situ*, and re-reduced *in situ* in the electron microscope in 1 mbar H_2 at 773 K for 30 min. Fig. 2b shows TEM images acquired *in situ* under these conditions. The images obtained at lower magnification show nanoparticles with an average diameter of 5.9 ± 1.2 nm, reflecting that the catalyst appeared thermally stable in the microscope. The insert is a high-resolution TEM image showing one representative particle with atomic lattice fringes extending across its projected area to the surfaces with distinct and straight facet terminations. Such profile-views of the surface terminations indicate that the organic ligands involved in the synthesis of the catalyst had been successfully

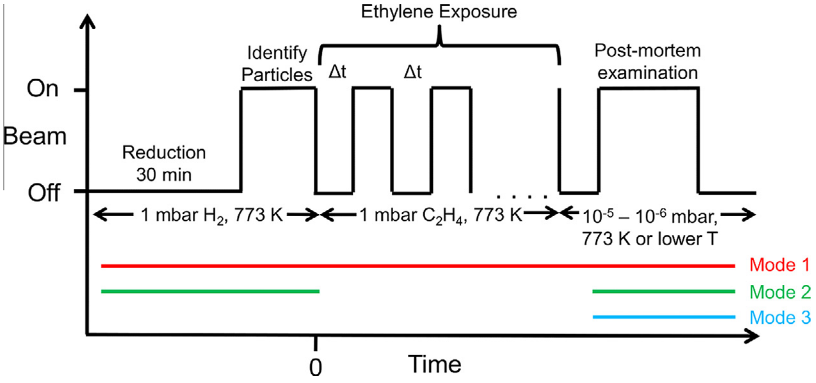

Fig. 1. Schematic of the experiment conducted *in situ* in a transmission electron microscope.

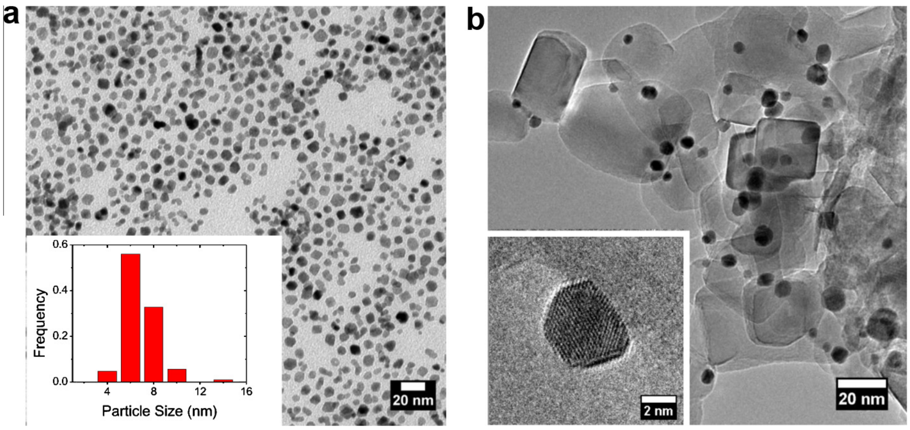

Fig. 2. (a) TEM image of as-synthesized Pt nanoparticles and their particle size distribution, and (b) TEM image of MgO-supported Pt acquired *in situ* in 1 mbar H_2 at 773 K after reduction at these conditions for 30 min. Inset of (b) shows one representative Pt particle taken at high resolution with an electron dose-rate of 2000 $e^-/(\text{Å}^2\ s)$.

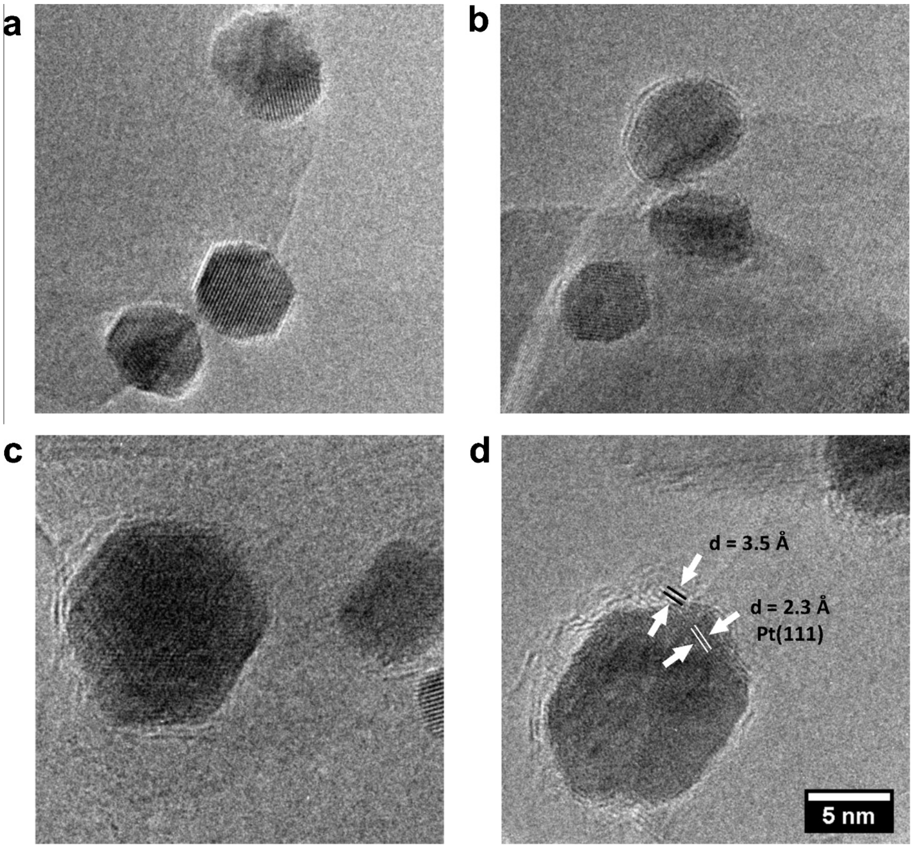

Fig. 3. *In situ* TEM images of Pt/MgO after 15 min exposure in 1 mbar C_2H_4 at (a) 623, (b) 673, (c) 723, (d) 773 K taken at 2000 $e^-/(Å^2 s)$, with the beam shut off during the growth process (Mode 3).

removed. The second sample (Fig. S1a) was synthesized by wet impregnation with the aim of attaining a larger average particle size in order to facilitate locating particles exhibiting carbon growth by encapsulation. It has been previously observed that carbon encapsulation on Pt occurs more prevalently on larger particles [20]. Fig. S1b shows an image of a representative particle after *in situ* reduction. It is evident that the Pt particle was also terminated by well-defined and clean facets. Throughout this study, both samples (Figs. 2 and S1) were used to track Pt particles that exhibited carbon encapsulation and similar dynamic behavior of the two samples was observed.

First, in order to address carbon deposition inherently related to Pt/MgO, a blind experiment was conducted. In this experiment, the catalyst was first reduced in H_2 at 773 K and then exposed to 1 mbar C_2H_4 for 15 min without beam illumination at a specified temperature, followed by evacuation of the gas and lowering of the temperature to 523 K for imaging. Fig. 3 shows that surface terminations observed in profile had additional layers of brighter contrast, corresponding to carbonaceous matter, and that the extent of this coke formation depended on temperature in the microscope. Below 623 K, no observable carbon was present on the Pt particles (Fig. 3a). However, coke formation was observed as the temperature was raised, as evidenced by a growing number of encapsulating carbon layers around the Pt particle. To conduct the carbon growth in a reasonable time window, a reaction temperature of 773 K was selected for the majority of the experiments reported here. It is worth noting that the measured spacing of the carbon layers was around 3.5 Å (Fig. 3d), which is larger than that of well-crystallized graphitic carbon (3.35 Å, JCPDS # 13-0148), suggesting that the carbonaceous deposits formed may not be fully devoid of hydrogen.

Next, to address the onset of the electron beam effect on growth, experiments were conducted under varying electron illumination conditions. In each experiment, at time zero, the reducing hydrogen gas had been replaced by 1 mbar of C_2H_4 and the temperature set to 773 K. In the following reaction time, a Pt nanoparticle was monitored by intermittent electron illumination at different electron dose-rates (mode 1). Fig. 4 reveals a marked effect of the electron illumination on the rate of carbon growth. The highest dose-rate used (2000 $e^-/(Å^2 s)$) provided images with the highest signal-to-noise ratio (S/N = 31.1) but at the cost of beam-inducing effects. After 16 min of reaction time at 2000 $e^-/(Å^2 s)$, the observed nanoparticle accumulated 4 layers of encapsulating carbon. However, at lower dose-rates (500 $e^-/(Å^2 s)$ and 1000 $e^-/(Å^2 s)$), significantly fewer layers formed at reaction times longer than 16 min. The S/N drops to 11.0 at 500 $e^-/(Å^2 s)$, which still captures carbon growth but at a lower sensitivity. Therefore, selection of the dose-rate appears to play an important role to ensure image quality while minimizing beam induced carbon growth. This qualitative effect observed in Fig. 4 can be quantified as shown in Fig. 5, where the number of full or partial layers of carbon is plotted as a function of reaction time for varying dose-rates. Again, it is clearly evident that using a dose-rate of 2000 $e^-/(Å^2 s)$ significantly enhances the rate of carbon growth compared to the lower dose-rates at which more comparable growth rates were observed, at similar total doses (Fig. 5 caption). The reference areas inspected after growth termination (Fig. S2) indicate that on particles previously unexposed by the beam, there is roughly the same number of layers of carbon as there were on the particles that were continuously imaged at both 1000 and 500 $e^-/(Å^2 s)$, whereas for Pt nanoparticles in the reference area shows less carbon compared to the particles illuminated by 2000 $e^-/(Å^2 s)$ through the experiment. Therefore, the two lower

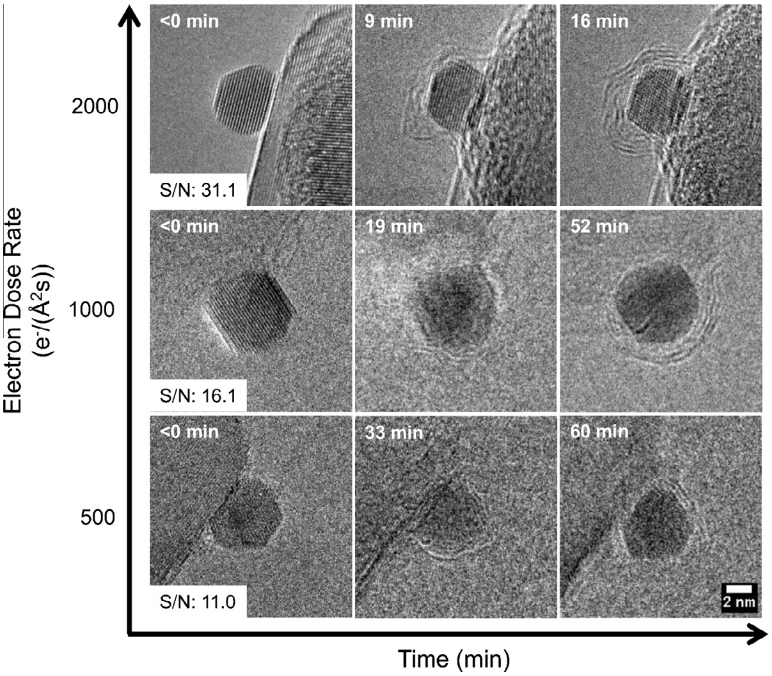

Fig. 4. Effect of the electron-beam dose-rate on carbon growth (1 mbar C_2H_4, 773 K) on Pt/MgO as a function of reaction time (Mode 1). For the 2000 $e^-/(Å^2\,s)$ series, the estimated electron doses are 3.6×10^5 $e^-/Å^2$ (9 min) and 7.2×10^5 $e^-/Å^2$ (16 min). For the 1000 $e^-/(Å^2\,s)$ series, the estimated electron doses are 1.2×10^5 $e^-/Å^2$ (19 min) and 2.4×10^5 $e^-/Å^2$ (52 min). For the 500 $e^-/(Å^2\,s)$ series, the estimated electron doses are 6×10^4 $e^-/Å^2$ (33 min) and 1.8×10^5 $e^-/Å^2$ (60 min). Images acquired at <0 min are under 1 mbar H_2, 773 K.

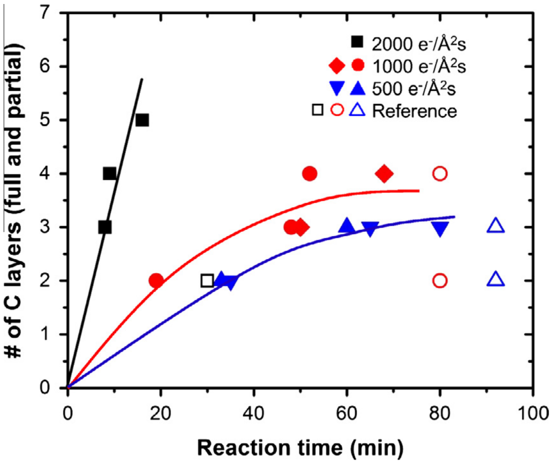

Fig. 5. The number of carbon layers (full + partial) on five Pt nanoparticles as a function of reaction time, under 1 mbar C_2H_4 and 773 K, at different dose-rates of 500, 1000 and 2000 $e^-/(Å^2\,s)$, respectively. Open symbols refer to other particles serving as a reference that were observed post-mortem (10^{-5} mbar and 773 K) without any prior beam exposure. Curves are included to guide the eye. The estimated electron doses are for the 2000 $e^-/(Å^2\,s)$ series (black square): 2.4×10^5 $e^-/Å^2$ (8 min), 3.6×10^5 $e^-/Å^2$ (9 min) and 7.2×10^5 $e^-/Å^2$ (16 min), for the 1000 $e^-/(Å^2\,s)$ series (red circle): 1.2×10^5 $e^-/Å^2$ (19 min), 1.8×10^5 $e^-/Å^2$ (48 min) and 2.4×10^5 $e^-/Å^2$ (52 min), for the 1000 $e^-/(Å^2\,s)$ series (red diamond): 1.2×10^5 $e^-/Å^2$ (50 min) and 2.4×10^5 $e^-/Å^2$ (68 min), for the 500 $e^-/(Å^2\,s)$ series (blue triangle up): 6×10^4 $e^-/Å^2$ (33 min) and 1.8×10^5 $e^-/Å^2$ (60 min), and for the 500 $e^-/(Å^2\,s)$ series (blue triangle down): 3×10^4 $e^-/Å^2$ (35 min), 9×10^4 $e^-/Å^2$ (65 min) and 1.5×10^5 $e^-/Å^2$ (80 min).

dose-rates were a suitable balance between maintaining a detectable image signal while suppressing beam-induced deposition.

This enhancement of the carbon growth rate by the electron dose-rate is likely due to the excitation or ionization of the reactant molecules via either primary or secondary electrons [50]. In addition to the dose-rate, the energy of the incident electrons may also impact growth. The present energy of 300 keV is higher than the threshold energy for atom displacement in carbon materials (ca. 68 kV) [51], so beam-induced sputtering off carbon may compete with the carbon deposition. This structural change was addressed by extended beam illumination of grown carbon structures in vacuum. Fig. 6 documents that the illumination during a period of 9 min at 1000 $e^-/(Å^2\,s)$ (a cumulative dose of 5.4×10^5 $e^-/Å^2$) is enough to sputter off two carbon layers. Therefore, it is important to limit the time of beam illumination when observing carbon in vacuum. During the *in situ* experiment, it is also inevitable that the electron beam may sputter off carbon concurrently with the carbon deposition. Thus, to address the significance of carbon sputtering, the total electron dose delivered to a specimen area under observation is estimated based on the dose-rate and accumulated illumination time. For image series discussed in the following, this estimated cumulative electron dose is kept at or below 5.4×10^5 $e^-/Å^2$ for reducing the impact of sputtering on carbon growth.

To address the mechanism of carbon growth, the first issue investigated was the growth mode of multiple carbon layers around the nanoparticle. From the two time series shown in Fig. 7, it is clear that multiple partial layers are capable of forming without the necessity of full particle encapsulation by the first layer. Examination of Fig. 7b and c (and similarly Fig. 7e and f) shows that additional layers of carbon have nucleated and grown from the surface of the observed nanoparticle, without the nanoparticle being fully encapsulated. Therefore, the formation of additional layers of carbon can precede the encapsulation of a Pt particle by a single layer. Due to the projection geometry in TEM imaging, surfaces other than those terminating the projected particle profile may form multiple carbon layers as well. Such layers remain unresolved due to the overlaid contrast from bulk nanoparticle and due to the low electron scattering power of C compared to Pt. However, to resolve details of the multi-layer growth mechanisms observations at the terminating surfaces are sufficient [28–30,32–34]. Moreover, part of the projected particle profiles

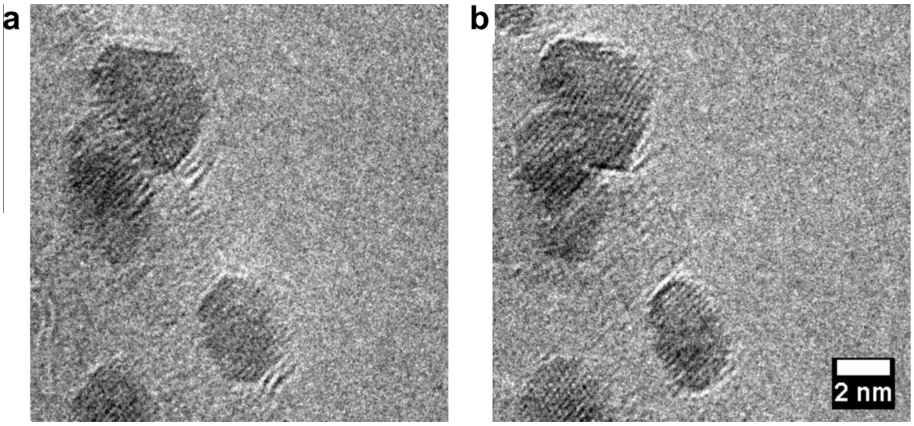

Fig. 6. Effect of beam illumination during post-mortem analysis on carbon deposited *in situ*. The (a) original carbon layers were sputtered off by the electron beam after (b) 9 min of illumination at 1000 e$^-$/(Å^2 s) at room temperature and 1.2×10^{-5} mbar.

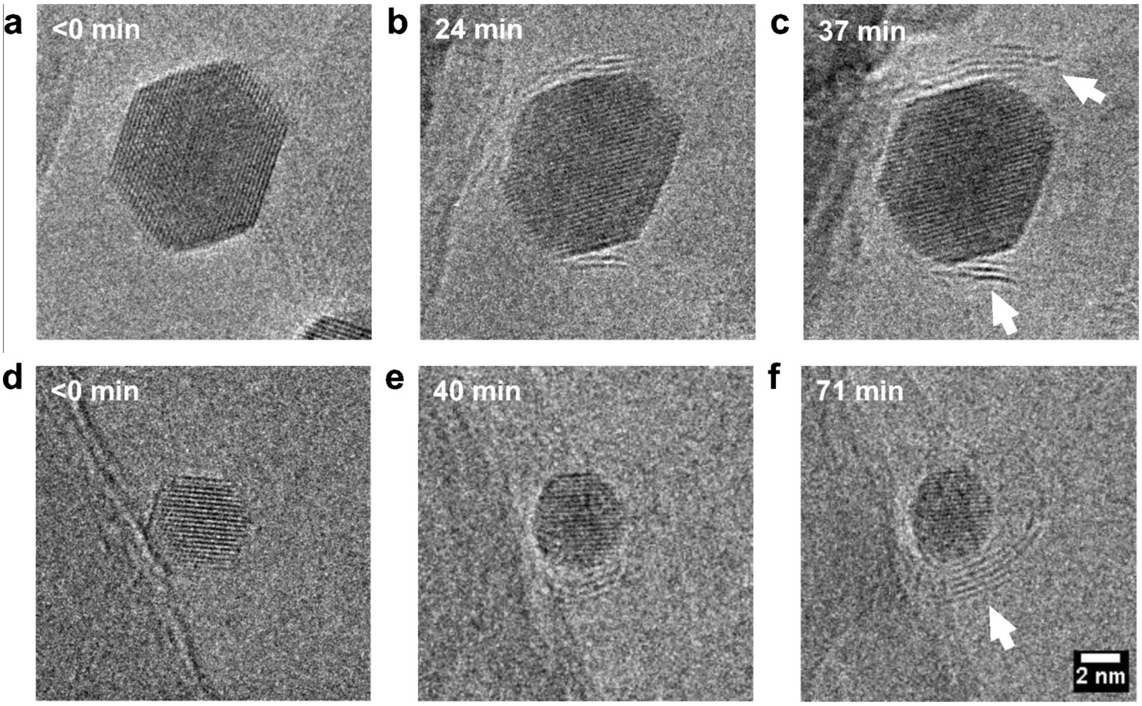

Fig. 7. Time-resolved TEM images showing multi-layer carbon growth on Pt nanoparticles. The images are extracted from image series acquired *in situ* in two experiments using mode 1 with $\Delta t \sim$ 15–30 min and shown versus reaction time. The images are recorded at 1000 e$^-$/(Å^2 s) (a–c) and 500 e$^-$/(Å^2 s) (d–f) and the estimated electron doses are (b) 1.8×10^5 e$^-$/Å^2, (c) 3.0×10^5 e$^-$/Å^2 and (e) 1.2×10^5 e$^-$/Å^2, (f) 1.8×10^5 e$^-$/Å^2. Growth conditions: 1 mbar C_2H_4, 773 K. The white arrows indicate the location of partial layer formation. Images acquired at <0 min are under 1 mbar H_2, 773 K.

remained unchanged and free of carbon during growth. This absence of carbon is likely due to either incomplete encapsulation of the gas-accessible Pt surface or parts of the particle periphery overlaid on the support in the image that reflects the Pt–MgO interface. No previous experimental evidence has directly addressed mechanisms for encapsulating Pt nanoparticles by multiple carbon layers, to the best of our knowledge. Interestingly, molecular dynamic (MD) simulations have shown that during the growth of the multiple carbon layers on Fe nanoparticles it is more favorable for carbon atoms deposited from the gas phase or precipitating from the nanoparticle to first complete an encapsulating carbon layer, after which carbon atoms precipitate from the bulk to form additional carbon layers between the existing layer and the metal nanoparticle surface [44]. To address the differences in the findings for Pt and Fe, a closer examination was undertaken of whether the Pt nanoparticle restructures over the course of carbon deposition.

A survey of three particles is shown in Fig. 8. It is clear that in each case the particles evolved in shape over time, and became rounder as the coking continued. While slight particle rotation during the course of the experiment could affect the profile shape of the particles, none of the particles observed became more facetted after carbon growth, suggesting that the “rounding” was inherent to the particle morphology. This reshaping is further corroborated by mapping out the projected shape of 15 different particles in their initial reduced state and after the carbon growth. For each state, the shape of the particle is simplistic parameterized by its circularity as calculated using Eq. (1).

$$\text{Circularity} = 4\pi \times (\text{area}/\text{perimeter}^2) \quad (1)$$

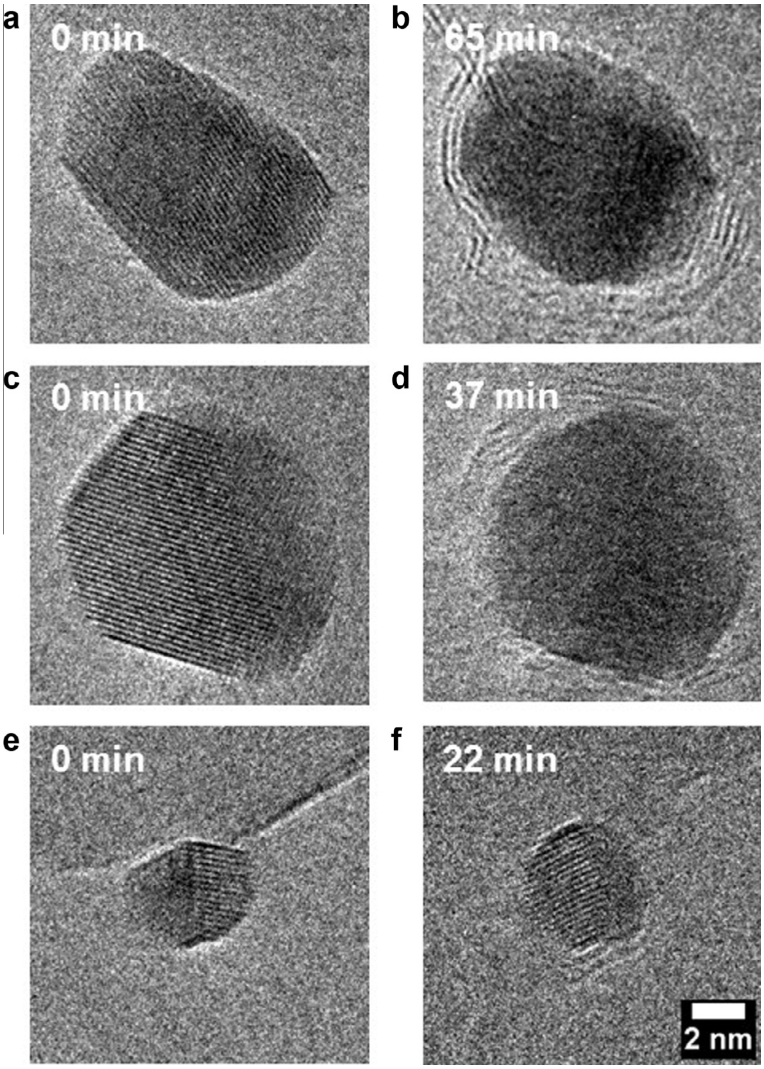

Fig. 8. *In situ* TEM images of three representative particles as a function of reaction time (a, c, e – 0 min, b – 65 min, d – 37 min, f – 22 min) illustrating shape change (Mode 1). The images are recorded at 1000 e$^-$/(Å^2 s) and the estimated electron doses are (b) 4.2 × 10^5 e$^-$/Å^2, (d) 3.0 × 10^5 e$^-$/Å^2, and (f) 1.2 × 10^5 e$^-$/Å^2. Growth conditions: 1 mbar C_2H_4, 773 K. Images acquired at <0 min are under 1 mbar H_2, 773 K.

With this definition, a circularity of 1.0 is expected for a perfect circle and a circularity of zero is expected for an infinitely elongated polygon. Fig. 9 shows that while the difference in circularity (Circularity$_{\text{post-reaction}}$ − Circularity$_{\text{initial}}$) was not uniform among all particles, all of the particles clearly became rounder as a function of reaction time. Absolute values of circularity for the 15 different particles are plotted as a function of reaction time in Fig. S3, with an example of a time-resolved series with labeled circularity values in Fig. S4. An increase in circularity implies the formation of more low-coordinated sites such as kinks, corners, and steps. Because of this evident restructuring of the nanoparticles, a greater focus was placed on the dynamics of the surface structure.

Fig. 10 shows a time series of TEM images illustrating the effect of carbon growth on the surface morphology of the Pt nanoparticle. At t = 3 min, we observe the formation of a partial layer of carbon on the topside of the nanoparticle, accompanied by the formation of a small step, and at t = 12 min, the formation of a second step appears at the bottom side of the nanoparticle together with the formation of another carbon layer. This effect becomes more pronounced over time as the step becomes enlarged at t = 20 min, allowing the formation of a second layer. This effect of step formation is in agreement with previous *in situ* studies of carbon nanofiber growth occurring on Ni [28–30]. However, for Pt, we see the formation of steps during carbon encapsulation. The formation of steps is further substantiated by the image series in Fig. 11. These image series therefore demonstrate that the surface of the

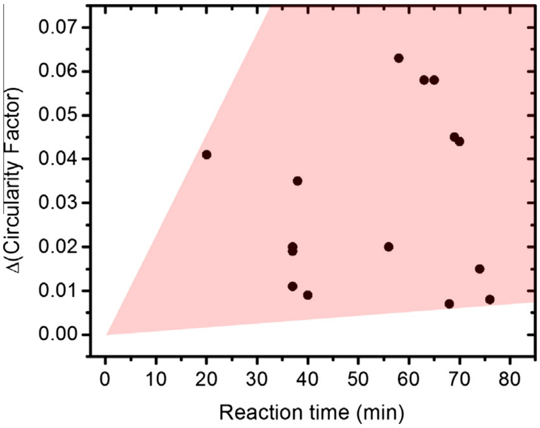

Fig. 9. Change in circularity factor (Circularity$_{\text{post-reaction}}$ − Circularity$_{\text{initial}}$) as a function of reaction time for 15 different particles, taken at 1000 e$^-$/(Å^2 s) and 500 e$^-$/(Å^2 s). Growth conditions: 1 mbar C_2H_4, 773 K.

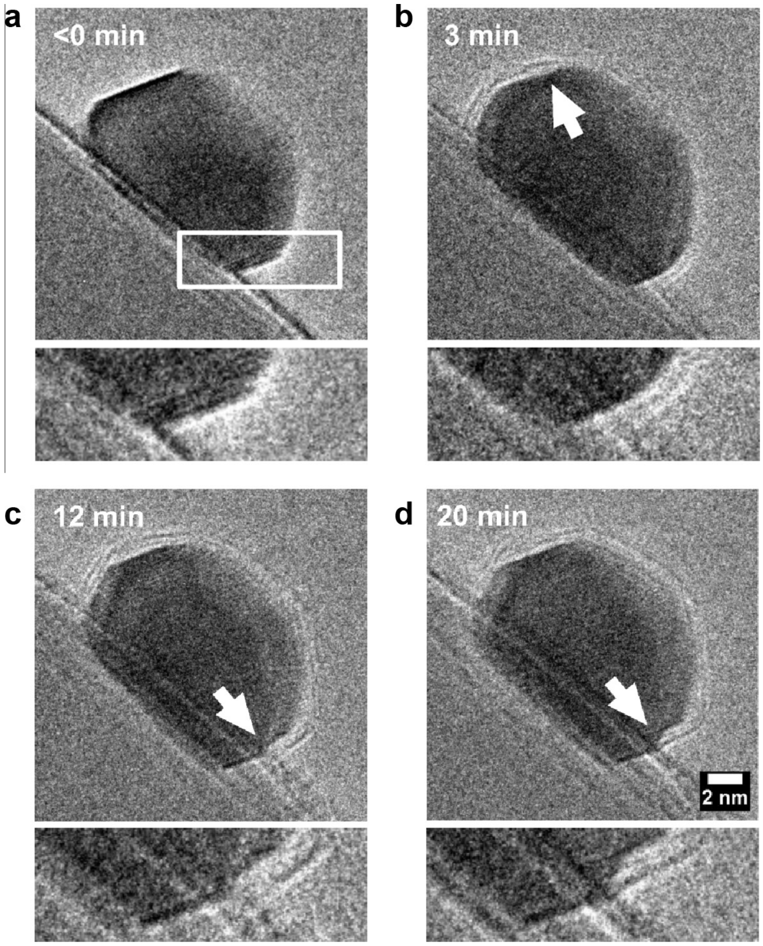

Fig. 10. Time-lapsed *in situ* TEM images of a Pt nanoparticle over the course of 20 min under 1 mbar C_2H_4 at 873 K. Images are recorded at 500 $e^-/(Å^2\ s)$ (Mode 1) and the estimated electron doses are (b) $6 \times 10^4\ e^-/Å^2$, (c) $1.8 \times 10^5\ e^-/Å^2$, and (d) $3.0 \times 10^5\ e^-/Å^2$. White arrows indicate the formation of a step accompanying carbon deposition and a region of interest (white box in (a)) enlarged below the image. Image acquired at <0 min is under 1 mbar H_2, 773 K.

nanoparticle changed over time due to the formation of new steps from which new carbon layers nucleated and grew. Therefore, as steps enlarged (Fig. 10) or multiple steps formed on the surface of the nanoparticle (Fig. 11), multiple new growth centers became available, explaining why multiple partial layers grew simultaneously. While it is possible that some facets contained steps in the reduced state, the overall constant periphery and overlap with the support in projected images of Figs. 10 and 11, indicate that the new steps are not a result of a particle rotation but rather a dynamic event in the course of time. Furthermore, we do not observe any apparent change in Pt nanoparticles under the exposure to only H_2 (Fig. S5), demonstrating that the electron illumination is not inducing atomic displacement under the present optical settings and exposure times and that step formation must be related to the ethylene exposure.

The question remains as to what is the driving force behind the restructuring of the Pt nanoparticle to form steps. For Ni, DFT calculations suggest that nucleation near a metal step edge is more likely than on a terrace site [28,37,39] and that the gain in energy by binding carbon atoms to a step compared to a terrace is enough to compensate the energy cost for Ni step formation. A similar explanation might be extended to Pt, though detailed DFT calculations for carbon growth on Pt are needed, which probably should consider the role of hydrogenated carbon species as well. While both Ni and Pt exhibit surface restructuring, carbon layers on Ni tend to slough off the particle and form a nanofiber [28], whereas Pt and other noble metals tend to exhibit carbon encapsulation [52]. In both cases, carbon layers tend to contour the surface of the nanoparticle. However, the Ni surface was dynamically changing upon step formation and restructuring such that the shape of the nanoparticles facilitated the alignment of the carbon layers into tubular structures. In contrast, the Pt surface was less fluctuating and the nanoparticle became encapsulated. The difference in dynamic behaviors is probably reflecting differences in the reaction conditions as well as the cohesive energy of the metals.

Previous *ex situ* TEM studies of carbon formation on Pt/MgO [20] have shown that the formation of carbon layers initiates at low-coordinated sites, such as steps, on the surface of Pt nanoparticles. Also of note, a recent study on the nucleation and growth of graphene on Pt(111) surfaces using scanning tunneling microscopy (STM) suggests that graphene islands nucleate slightly more favorably at metal step edges than on terraces [53]. Therefore, a possible explanation for why bimetallic Pt catalysts are effective at suppressing coke deposition is that the second element (Sn, In, Ga, etc.) increases the strain at the Pt step edge and suppresses the nucleation of carbons at the steps [38]. It is important to note, however, that not all particles observed in the present study exhibited step formation in conjunction with carbon growth. This could be either a result of carbon nucleating on a terrace site, consistent with Ref. [53], or a step site that is hidden from a 2-D projection view of a 3-D nanoparticle. It is evident, though, that the nanoparticls are not static during coking deposition (Fig. 8), and in some cases, step formation facilitates the nucleation and growth of additional carbon layers (Figs. 10 and 11).

Despite the “pressure gap” between experiments done in a reactor system and inside the microscope, similarities in step

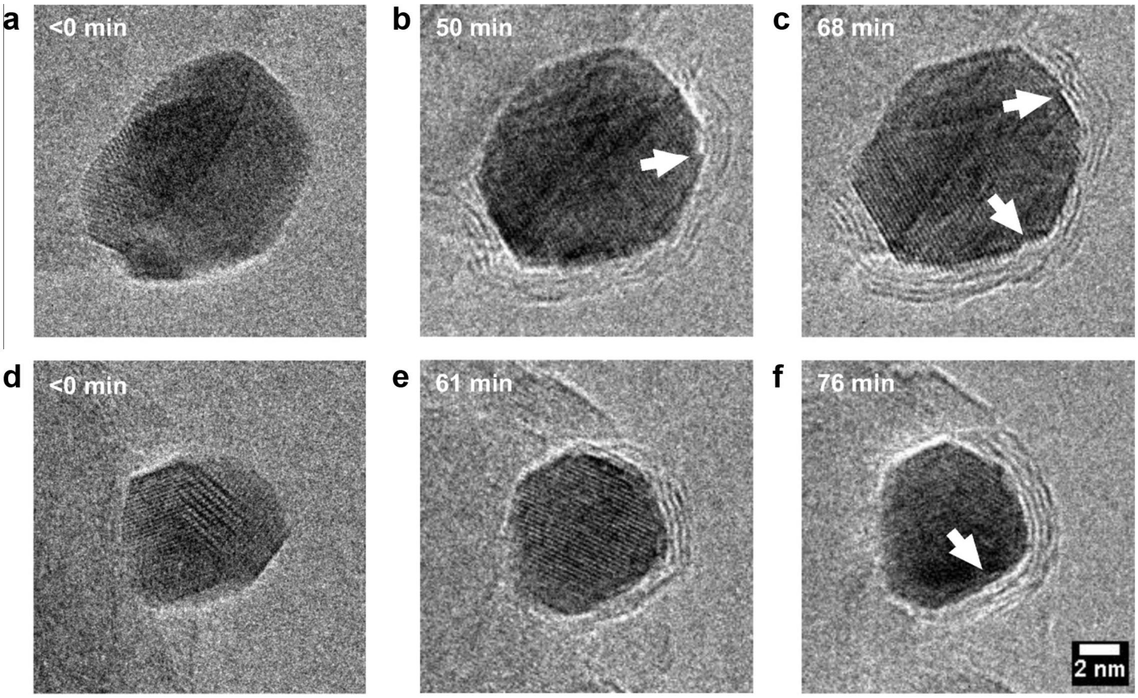

Fig. 11. Two time-lapsed series of TEM images of (a – 0 min, b – 50 min, c – 68 min, and d – 0 min, e – 61 min, f – 76 min) of Pt nanoparticles as a function of reaction time during carbon growth (1 mbar C_2H_4, 773 K). Images are recorded at 1000 $e^-/(Å^2\ s)$ (Mode 1) and the estimated electron doses are (b) $2.4 \times 10^5\ e^-/Å^2$, (c) $4.2 \times 10^5\ e^-/Å^2$, (e) $2.4 \times 10^5\ e^-/Å^2$, and (f) $3.6 \times 10^5\ e^-/Å^2$. White arrows indicate the location of step formation as carbon layers encapsulate the nanoparticle. Images acquired at <0 min are under 1 mbar H_2, 773 K.

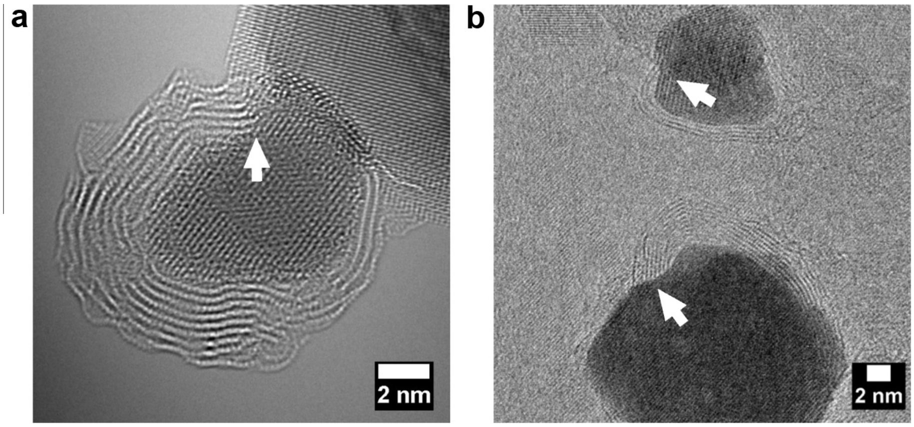

Fig. 12. An *ex situ* TEM image of (a) Pt/MgO carburized in a reactor system under 0.2 bar ethane at 873 K for 1 h. For comparison, an *in situ* TEM image of (b) Pt/MgO carburized in the microscope under 1 mbar C_2H_4 at 773 K for 20 min, taken at 500 $e^-/(Å^2\ s)$ (Mode 3).

formation and carbon nucleation are striking, as shown in Fig. 12. In Fig. 12a, a sample of Pt/MgO had been exposed to a pressure of 0.4 bar of ethane for 2 h at 873 K and imaged *ex situ* by HRTEM. The carbon layers can be traced back to the step that has formed on the concave side of the nanoparticle. Nanoparticles that had been exposed to 1 mbar of ethylene for 20 min at 773 K (Fig. 12b) exhibited almost identical characteristics, with multiple carbon layers nucleating from the step edge. Therefore, despite the low pressures of hydrocarbon used in the *in situ* TEM experiment, similarities in carbon growth mechanisms can be observed, proving *in situ* TEM is a valuable tool for imaging catalysts at work.

4. Conclusion

In situ HRTEM experiments were done to investigate the formation of carbon layers on MgO-supported Pt nanoparticles upon exposure of the catalyst to ethylene at elevated temperature. An imaging strategy was carefully established in order to suppress beam-assisted carbon growth and to minimize beam-induced sputtering of grown carbon layers. Hereby, *in situ* TEM reveals that multiple partial layers of carbon formed without the Pt particle being completely encapsulated by the first carbon layer. Additionally, particles became rounder as a function of reaction time, suggesting that coking caused significant restructuring on Pt nanoparticles. A closer look at the surface of the nanoparticles revealed that, in some cases, steps formed spontaneously in the surface and assisted in nucleation and growth of multiple carbon layers involved with the encapsulation of nanoparticles.

Acknowledgments

This work was supported by a grant from Chevron Energy Technology Company. *Ex situ* microscopy experiments were conducted at the UC Berkeley Electron Microscopy Lab and the Molecular

Foundry, Lawrence Berkeley National Lab, which is supported by the U.S. Department of Energy under Contract # DE-AC02-05CH11231. The authors express their appreciation for the opportunity to obtain *in situ* TEM images at Haldor Topsoe A/S. The authors also acknowledge Hanne Falsig, Juan Salvador Martinez Espin and Pablo Beato for fruitful discussions and support.

Appendix A. Supplementary material

Supplementary data associated with this article can be found, in the online version, at http://dx.doi.org/10.1016/j.jcat.2016.03.010.

References

[1] D.E. Resasco, Dehydrogenation – heterogeneous, Encyclopedia of Catalysis (2002).
[2] J. Wu, Z. Peng, A.T. Bell, J. Catal. 311 (2014) 161–168.
[3] R.D. Cortright, J.M. Hill, J.A. Dumesic, Catal. Today 55 (2000) 213–223.
[4] M. Findlater, J. Choi, A.S. Goldman, M. Brookhart, Catal. Met. Complexes 38 (2012) 113–141.
[5] G.C. Bond, R.H. Cunningham, J. Catal. 166 (1997) 172–185.
[6] R.J. Davis, E.G. Derouane, Nature 349 (1991) 313–315.
[7] J. Zheng, J.L. Dong, Q.H. Xu, Y. Liu, A.Z. Yan, Appl. Catal. A 126 (1995) 141–152.
[8] Y. Barron, D. Cornet, G. Maire, F.G. Gault, J. Catal. 5 (1996) 428–445.
[9] F. Garin, S. Aeiyach, P. Legare, G. Maire, J. Catal. 77 (1982) 323–337.
[10] J. Barbier, G. Corro, Y. Zhang, Appl. Catal. 13 (1985) 245–255.
[11] G.F. Fremont, Catal. Rev. 50 (2008) 1–18.
[12] Z. Paal, A. Wootsch, R. Schlogl, U. Wild, Appl. Catal. A: Gen. 282 (2005) 135–145.
[13] P. Sun, P. Sun, G. Siddiqi, W.C. Vining, M.F. Chi, A.T. Bell, J. Catal. 282 (2011) 165–174.
[14] N.A. Pakhomov, Kinet. Catal. 42 (2001) 334–343.
[15] M. Breysse, P. Afanasiev, C. Geantet, M. Vrinat, Catal. Today 86 (2000) 5–16.
[16] J. Barbier, Appl. Catal. 23 (1986) 225–243.
[17] J. Barbier, G. Corro, Y. Zhang, J.P. Bournonville, J.P. Franck, Appl. Catal. 13 (1985) 245–255.
[18] J. Barbier, G. Corro, Y. Zhang, J.P. Bournonville, J.P. Franck, Appl. Catal. 16 (1985) 169–177.
[19] J. Barbier, E. Churin, P. Marecot, J.C. Menezo, Appl. Catal. 36 (1988) 277–285.
[20] Z. Peng, F. Somodi, S. Helveg, C. Kisielowski, P. Specht, A.T. Bell, J. Catal. 286 (2012) 22–29.
[21] P. Gallezot, C. Leclercq, M. Guisnet, P. Magnoux, J. Catal. 114 (1988) 100–111.
[22] E.E. Wolf, F. Alfani, Catal. Rev. Sci. Eng. 24 (1982) 329–371.
[23] F. Frusteri, L. Spadaro, F. Arena, A. Chuvilin, Carbon 40 (2002) 1063–1070.
[24] R.T.K. Baker, P.S. Harris, J. Phys. E: Sci. Instrum. 5 (1972) 793–797.
[25] E.D. Boyes, P.L. Gai, Ultramicroscopy 67 (1997) 219–232.
[26] P.L. Hansen, J.B. Wagner, S. Helveg, J.R. Rostrup-Nielsen, B.S. Clausen, H. Topsøe, Science 295 (2002) 2053–2055.
[27] J.R. Jinschek, Chem. Commun. 50 (2014) 2696–2706.
[28] S. Helveg, C. Lopez-Cartes, J. Sehested, P.L. Hansen, B.S. Clausen, J.R. Rostrup-Nielsen, F. Abild-Pedersen, J.K. Nørskov, Nature 427 (2004) 426–429.
[29] S. Hofmann, R. Sharma, C. Ducati, G. Du, C. Mattevi, C. Cepek, M. Cantoro, S. Pisana, A. Parvez, F. Cervantes-Sodi, A.C. Ferrari, R. Dunin-Borkowski, S. Lizzit, L. Petaccia, A. Goldoni, J. Robertson, Nano Lett. 7 (2007) 602–608.
[30] M. Lin, J.P.Y. Tan, C. Boothroyd, K.P. Loh, E.S. Tok, Y.L. Foo, Nano Lett. 6 (2006) 449–452.
[31] R.T.K. Baker, P.S. Harris, R.B. Thomas, R.J. Waite, J. Catal. 26 (1972) 51–62; R.T.K. Baker, P.S. Harris, R.B. Thomas, R.J. Waite, J. Catal. 30 (1973) 86–95.
[32] R. Sharma, E. Moore, P. Rez, M.M.J. Treacy, Nano Lett. 9 (2009) 689–694.
[33] H. Yoshida, S. Takeda, T. Uchiyama, H. Kohno, Y. Homma, Nano Lett. 8 (2008) 2082–2086.
[34] M. Picher, P.A. Lin, J.L. Gomez-Ballesteros, P.B. Balbuena, R. Sharma, Nano Lett. 14 (2014) 6104–6108.
[35] R. Schlögl, Adv. Catal. 56 (2013) 103–185.
[36] J. Gao, J. Yip, J. Zhao, B. Yakobson, F. Ding, J. Am. Chem. Soc. 133 (2011) 5009–5015.
[37] H.S. Bengaard, J.K. Nørskov, J. Sehested, B.S. Clausen, L.P. Nielsen, A.M. Molenbroek, J.R. Rostrup-Nielsen, J. Catal. 209 (2002) 365–384.
[38] S. Saadi, F. Abild-Pedersen, S. Helveg, J. Sehested, B. Hinnemann, C.C. Appel, J.K. Nørskov, J. Phys. Chem. C 114 (2010) 11221–11227.
[39] F. Abild-Pedersen, J.K. Nørskov, J.R. Rostrup-Nielsen, J. Sehested, S. Helveg, Phys. Rev. B 73 (2006) 115419.
[40] J.R. Rostrup-Nielsen, D.L. Trimm, J. Catal. 48 (1977) 155–165.
[41] W.T. Owens, N.M. Rodriguez, R.T.K. Baker, J. Phys. Chem. 96 (1992) 5048–5053.
[42] T.S. Chang, N.M. Rodriguez, R.T.K. Baker, J. Catal. 123 (1990) 486–495.
[43] B.J. Kang, J.H. Mun, C.Y. Hwang, B.J. Cho, Appl. Phys. 106 (2009) 104309.
[44] F. Ding, A. Rosen, E.E.B. Campbell, L.K.L. Falk, K. Bolton, J. Phys. Chem. B 110 (2006) 7666–7670.
[45] V. Galvita, G. Siddiqi, P. Sun, A.T. Bell, J. Catal. 271 (2010) 209–219.
[46] J.R. Jinschek, S. Helveg, Micron 43 (2012) 1156–1168.
[47] F. Somodi, Z. Peng, A. Getsoian, A.T. Bell, J. Phys. Chem. C 115 (2011) 19084–19090.
[48] P.L. Hansen, S. Helveg, A.K. Datye, Adv. Catal. 50 (2006) 77–95.
[49] L.P. Hansen, E. Johnson, M. Brorson, S. Helveg, J. Phys. Chem. C 118 (2014) 22768–22773.
[50] W.F. van Dorp, C.W. Hagen, J. Appl. Phys. 104 (2008) 081301.
[51] R.F. Egerton, R. McLeod, F. Wang, M. Malac, Ultramicroscopy 110 (2010) 991–997.
[52] S. Helveg, J. Sehested, J.R. Rostrup-Nielsen, Catal. Today 178 (2011) 42–46.
[53] X. Feng, J. Wu, A.T. Bell, M. Salmeron, J. Phys. Chem. C 119 (2015) 7124–7129.